Mechanical behavior of embedded bistable dome shell with tunable energy barrier asymmetry

Frédéric Albertini [a,b,*], M. Gabriella Tarantino [c], Laurent Daniel [a,b]

[a] *Université Paris-Saclay, CentraleSupélec, CNRS, Laboratoire de Génie Electrique et Electronique de Paris, 91192, Gif-sur-Yvette, France*
[b] *Sorbonne Université, CNRS, Laboratoire de Génie Electrique et Electronique de Paris, 75252, Paris, France*
[c] *Université Paris-Saclay, ICMMO/SP2M, CNRS, 91405 Orsay, France*

A B S T R A C T

In this work, the mechanical response at finite strains of embedded dome shells is investigated both numerically and experimentally. These systems are interesting as they exhibit up to two stable shapes, a feature that makes them promising candidates for numerous applications from energy harvesting to shape morphing. The energy landscape scenario of these structures presents a major peculiarity as the strain energy required to switch the system between its stable shapes is path-dependent and varies upon loading (i.e. *snap-through instability*) and unloading (i.e. *snap-back instability)*. This paper proposes to investigate their asymmetrical mechanical behavior. To do so, Finite Element computations were first carried out onto dome shell models, where the geometrical parameters were varied systematically. Specifically, two sets of computations were conducted using the Static Damping Method. The first served to identify the mono- and bistable domains of the embedded dome shells as function of the dome main geometrical parameters. The second focused on bistable dome geometries and explored systematically the asymmetry in the *energy barrier* required to switch between the two equilibrium states. Interestingly, the results of this study showed that a simple asymmetry indicator could be used to effectively qualify the dome asymmetric bistability, in turn providing simple guidelines for the design of morphing structures with programmable response. Finally, in order to validate the numerical results, the mechanical response of the 3D-printed rubber-like dome shells was measured experimentally using a dedicated set-up that was designed and fabricated to this purpose. The results of experiments were found to be in good agreement with those of simulations.

1. Introduction

Mechanical instabilities have been avoided for long time by mechanical engineers and designers, as they have often been considered the precursor of the structure catastrophic failure. However, in the last decade many studies have demonstrated that instabilities can be harnessed to attain new properties and functionalities [1–3]. These include notably a superior damping [4] and load-bearing capacity [5] in composites that contain negative stiffness elements [6], as well as non-conventional pattern transformations in rubber-like porous structures with a periodic design [7,8]. Likewise, structures can also take advantage of mechanical instabilities to achieve programmable shape morphing capabilities [9,10]. In very recent years, the rapid progress in 3D-printing technology has enabled the design of materials and structures that encode a variety of shape change functionalities. Mechanical metamaterials – as these materials are also called – have a tailored architecture optimized across different length scales, and can showcase

morphing capabilities that are reminiscent of those displayed by living organisms (e.g. plants and animals). To date, mechanical metamaterials with programmable shape-changing capabilities have been designed and used to control, e.g., the propagation of elastic waves in flexible structures [11–13] , or to enable tunable actuation in soft robots and bio-inspired systems [14–16].

Another important feature resulting from structural instabilities is multi-stability [17]. The latter is characterized by the presence of more than one minimum in the energy landscape and allows a structure to have multiple stable configurations. Multistable systems prove therefore highly suitable for application in smart systems and can be designed to exhibit tunable properties (e.g. energy dissipation and thermal expansion [18–20]) and programmable shapes in response to an external stimulus [21,22]. Most synthetic morphing systems realized to date are bistable mechanisms, whereby typical designs employ either bending laminates [23–26] or axially-prestressed

beams [19,20,27–30] to achieve snapping between two distinct stable shapes. Multistability in these systems is of geometrical origin and arises from the structure's hierarchical architecture, whereby elastic instability (e.g. bucking in beams) at the meso-scale enables obtaining different programmable shapes at the macro-scale. Notable, yet very recent, examples of multistable structures include shape memory polymer shells [25], elastomeric beams comprising multiple self-similar modules [8] as well as thermoplastic dome-patterned structures [31–33]. By virtue of their tunable response, these examples encourage the pursuit of novel multistable structures that derive functionality from mechanical instability.

Doubly curved shells, namely *domes*, provide an attractive gateway towards the design of multistable morphing systems. Their simple geometry exhibits a bistable behavior and can be patterned into a variety of structures, from 1D to 3D [31–33]. Moreover, dome arrays can be fabricated at any structural scale, including the micrometric [34] and the nanometric scale [35]. To date, bistable domes have been used in many applications. For example, dome-patterned structures have been employed to obtain tunable optical properties [34], adaptive stiffness [32] and tunable energy dissipation [36] as well as shape programmability and robotic actuation [31,37]. Dome shells are structures that exhibit multi-stable behavior and they can display up to two stable states. They have been studied for decades, while one of the first investigation of the buckling and post-buckling behavior of thin spherical caps has been conducted by Brodland and Cohen [38], using numerical and experimental analysis. These authors investigated the physical origin of bistability of dome shells focusing on their geometry, and used a geometric dimensionless parameter to analyze and compare the behavior of different shells. Notably, bistability of dome shells results from an equilibrium between stretching and bending energies during shell deformation. Stating that the elastic response of a shell can be decomposed into membrane and bending effects, Kaplan et al. [39] introduced a geometric dimensionless parameter λ as the ratio of membrane energy (governed by stretching) over bending energy. This ratio is defined as the fourth root of its original definition [38], i.e.:

$$\lambda = \sqrt[4]{\frac{U_{stretching}}{U_{bending}}} = \sqrt[4]{12(1-\nu^2)}\sqrt{\frac{R}{h}}\alpha \tag{1}$$

With ν the constitutive material Poisson's ratio, R the dome radius, h the shell thickness and α the dome half-angle. From λ definition in Eq. (1), one can infer that bistability of a dome relies mostly on geometric parameters R, h and α, but also on the constitutive material parameter ν. Specifically, the influence of the Poisson's ratio and shell thickness on spherical dome stability was exhaustively demonstrated by Madhukar [40]. Because of its simple definition and physical derivation, the dome parameter λ has been largely used as an effective criterion to discriminate bistable from monostable configurations. The recent study by Taffetani et al. [41] provides a quantitative analysis onto the geometric parameter threshold between monostable and bistable domains. The bistability of a dome shell also depends on several other parameters that are not accounted for by Eq. (1). These are both geometry- and material-dependent. Notably, Sobota et al. [42] have shown that the bistability of a dome shell depends on the boundary conditions applied at the edge of the shell, while Wan et al. [43] have investigated the influence of geometric defects. Equally important, time-dependent bistability, often called pseudo-bistability [33], can be encountered for visco-elastic shells [44] as the relaxation changes the stretching to bending energy ratio.

The bistable response of dome shells also changes when these structures are integrated, i.e. *embedded* into larger objects or systems. This has been shown, e.g., by Liu et al. who studied the mechanical behavior of a single embedded dome unit, called a snappit [45]. Notably, they demonstrated that the stability domains not only rely on dome shell geometric parameters and constitutive material as stated by Eq. (1), but also on the distance to the boundary conditions. Embedded bistable domes are of great practical interest as they can be used, e.g., to design bistable valve for soft robotics [46], valve with passive flow control [47], bioinspired reconfigurable soft robot [48], programmable grippers [49,50] or even soft pneumatic digital logic gates [51]. However, the knowledge of the required energy to switch between stability states, often referred to as the *energy barrier*, is instrumental to design such systems. To provide a quantitative measure of how difficult it is to transition from one stability state to another, Mukherjee et al. [52] qualified such required energy as the strength of stability. However, the quantification of the stability strength is often not straightforward as the energy landscape of a system, including embedded domes, depends on numerous factors. Likewise, the energy needed to transition between two different stability states can be either symmetric, when the depth of the energy wells are equal, or asymmetric in the opposite case. This is schematically illustrated in Fig. 1. The quantification of the *energy barrier* and notably of its possible asymmetric nature, is in turn of crucial importance to choose the proper actuation mechanism to switch between two stable states. Yet, while prior work has widely explored effective actuation strategies for dome-based structures (e.g. via embedded magnetic particles [53,54] or by chemical routes [55]), only a few studies have investigated the asymmetric nature of the energy landscape of dome shells [40]. At present, and to the best of our knowledge, a systematic investigation of the asymmetric bistable response of embedded domes has not yet been conducted. This is what we propose here to do.

The present paper investigates both numerically and experimentally the energy landscape of embedded dome shells whose geometrical parameters are varied systematically. Notably, its main focus is to quantify by mean of a simple index the asymmetry of the strain energy *strength* (i.e. threshold) to switch from the two equilibrium states. The latter in turn can provide simple guidelines for the design of novel bistable dome shells with tunable shape switch. Specifically, the paper is organized as follows. In Section 2 the methods used for both experiments and simulations are first presented and the constitutive law for the material used for manufacturing the test samples is provided. The results of both experiments and simulations are then presented in Section 3. Notably, two sets of numerical results are reported. The first focuses on the parametric study of the mono- and bistability domains (Section 2.4.1) and is complemented with selected experimental results of the dome mechanical behavior; the second investigates the asymmetry of the transition between the two equilibrium states for a variety of bistable dome geometries (Section 3.3). Conclusion are given in Section 4.

2. Materials and methods

This section provides a description of the materials and methods used throughout the study. Specifically, it starts with the definition of the geometric parameters used to design the embedded dome shells (Section 2.1) and the description of the material model (Section 2.2). The numerical framework used to ensure numerical convergence is detailed in Section 2.3, while the Boundary Conditions (BCs) used for FE analysis are described in Section 2.4 as well as the detailed organization of the numerical computations. Experimental samples manufacturing is presented in Section 2.5.1, and a description of the experimental set-up and protocols is given in Section 2.5.2.

2.1. Dome shell model definition

The dome shell structure studied in this work consists of a thin dome encircled by a circular plate, as sketched in Fig. 2(a). A detailed illustration of the dome shell geometric parameters is presented in Fig. 2(b). Three parameters are notably used to define the dome geometry: the inner radius R, the shell thickness h (uniform throughout the structure) and the half-angle α. In particular, the *deepness* of a dome shell depends
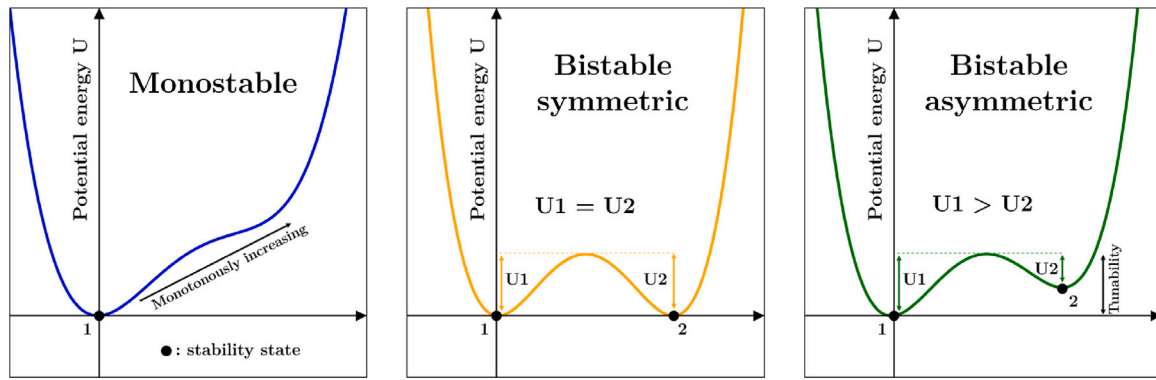
Fig. 1. Energy landscapes associated with monostable, symmetric bistable and asymmetric bistable systems. Bistable systems can present symmetric (with two equally deep energy wells) or asymmetric (with two unequally deep energy wells) landscape depending on their configuration. The present work investigates the reasons behind the asymmetric behavior of embedded dome shells and explores the tunability of the landscape asymmetry.
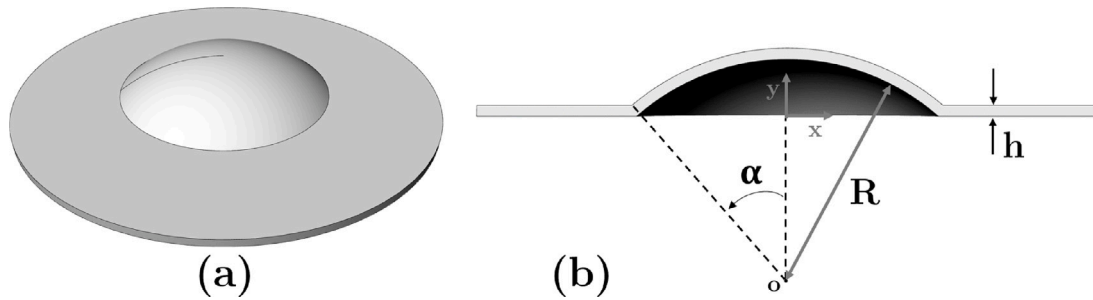

Fig. 2. Dome shell model definition: (a) isometric view ; (b) cross section with illustration of the geometric parameter explored in this study: R is the inner dome radius, h is the shell thickness (constant all over the model), and α the dome half-angle.

Table 1
Values of the geometrical parameters explored in this study for the dome inner radius R, shell thickness h and half-angle α. The latter is discretely varied between 0° and 90°.

Parameter (unit)	Values
Inner dome radius R (mm)	[10; 15; 20]
Dome half-angle α (°)	[0–90]
Shell thickness h (mm)	[0.5; 0.75; 1]

on the parameter α, which is used in the literature [41,42], to discriminate between *shallow* and *deep* domes, corresponding respectively to small and large values of this parameter. For practical purposes and notably in order to ease experiments, this study focuses on thin shells that can be handily manipulated and reconfigured. Consequently, dome sizes are designed close to roughly the size of a human finger: inner dome radii R are chosen to vary between 10 and 20 mm, whereas values of the thickness h between 0.5 and 1 mm and of the dome half-angle α between 0° and 90° are explored. A summary of the studied geometric parameters values is reported in Table 1.

2.2. Material

To investigate the bistable behavior of the domes both in experiments and simulations, the chosen constituent material is a rubber-like photocurable resin that goes under the commercial name TangoBlack FLX 930 (Stratasys, France). To date, such polymer material has been used to produce different types of highly deformable structures such as porous Voronoi-type materials [56] and hierarchical beams [8]. TangoBlack FLX 930 has a hyperelastic behavior and its constitutive law has been modeled using the Neo-Hookean model [57], implemented in Abaqus FE commercial software [58].

This model is described using a strain energy potential function that depends on both the deviatoric and volumetric component of the strain

invariants, i.e. :

$$W = C_{10}(I_1 - 3) + \frac{1}{D_1}(J^{el} - 1)^2 \qquad (2)$$

where I_1 is the first strain invariant and J^{el} is the elastic volume strain which accounts for the total and thermal volume strains. A detailed explanation of the constitutive law provided by Eq. (2) is given in Abaqus documentation [58]. C_{10} and D_1 are related to the material shear and bulk moduli: $\mu_0 = 2C_{10}$; $K_0 = \frac{2}{D_1}$. Experimentally measured values for these two parameters reported in the literature [8] are used in this study, namely $C_{10} = 0.6$ MPa; $D_1 = 1.10^{-6}$ MPa. It is noted in passing that the constitutive material behavior considered in this study does not account for visco-elastic properties, hence pseudo-bistability of dome shells is not examined.

2.3. Numerical framework

In this work, numerical simulations were performed using the commercial FE solver Abaqus (Dassault Systems) with standard implicit formulation. Prior to describing the computational experiments carried out to investigate bistability of embedded dome shells, the numerical framework is presented hereinafter. All simulations were carried out in a finite-strain setting, whereby the effects of geometric nonlinearity were accounted for via the Abaqus command *NLGEO. Different numerical methods have been exploited in prior works to study buckling or snapping of structures. These include the Riks algorithm [40,59], the Static Damping Method [40,45,60] as well as the implicit dynamic analysis [33,45]. For the sake of completeness, it is noted in passing that analytical approches have also been employed to study mechanical instabilities [41,42] but have not been explored in the present work. Here, the Static Damping Method is used to run the simulations. This method consists in adding an artificial global damping coefficient in

non-linear static analysis [60] in order to prevent fast dynamic displacement during buckling. The damping forces are calculated as follows:

$$F_v = \mu M (u/\Delta t) \tag{3}$$

With F_v being the viscous damping force, μ the damping coefficient, M the artificial mass matrix, u the displacement matrix and Δt the time increment. This strategy is considered valid if the damping energy remains small when compared to the strain energy computed at each time increment during the numerical simulation.

Prior to run the simulations, a convergence study has therefore been conducted in order to find the damping coefficient μ that minimizes the influence of damping on the FE results while ensuring computational convergence. This study has been performed on selected embedded dome shell configurations, whereby only μ was varied. The values obtained for the damping coefficient μ are comprised between $\mu = 1 * 10^{-7}$ and $1 * 10^{-8}$ (depending on the deepness of the shell), and are in agreement with prior studies on multistable structures [32,45]. The present numerical framework based on the Static Damping Method has been employed to run all computational experiments of this work. The latter are described in what follows.

2.4. Computational experiments

Computational experiments have been conducted using the previously described numerical framework. Two different sets of FE simulations were performed for the range of embedded dome shell parameters reported in Table 1, namely (i) a stability analysis and (ii) a strain energy asymmetry analysis. The former was carried out with the goal of identifying the bistable and monostable domains. The latter was performed with the aim of quantifying the so-called *energy barrier*, namely the strain energy required to switch from one stable state to another. Its ultimate goal was to identify the combination of dome shell geometrical parameters for which the transition between the two stable states is strongly asymmetric (see Fig. 1). The results of the computational experiments are discussed in Section 3 and aim to provide a novel roadmap for the design of embedded dome shells with tunable transition between two stable states.

To trigger instability and thus to study the mechanical response of the dome shells, the loading was modeled by imposing a vertical displacement along the y direction (see Fig. 2) at the top of the dome shell, while the latter was clamped along its outer circular plate. The applied boundary conditions (BCs) and loading are schematically reported in Fig. 3. As seen, the displacement δ_y was applied onto a small circular area of radius 1 mm at the top of the dome. Numerically, this was accomplished by imposing a kinematic coupling between the nodes of the circular region (highlighted with red color in Fig. 3) and a control point arbitrarily defined (with all DOFs constrained). Because of the small finite-size area chosen to apply δ_y, it is legitimate to assume that the deformation of the shell remains fairly axisymmetric. The clamped BCs were imposed at a distance D from the center of the dome. Clamped BCs were chosen in order to reproduce the integration of dome shell in a system. The clamping distance D is calculated proportionally to the lateral size of the dome, designated as L in Fig. 3(b). In this study a constant ratio of $D/L = 1.5$ was used throughout the numerical analysis.

2.4.1. Stability analysis

Prior to describing how the stability analysis onto the dome shells was conducted, the basic lexicon of a curved shell bistability is hereinafter recalled. Specifically, the two stable shapes of the embedded dome are defined respectively as *original* and *everted*, see Fig. 4. The former corresponds to the natural dome shape, the latter to the inverted equilibrium shape achieved upon snap-through instability. For a curved shell system, *snap-through* instability is associated with the rapid transition between the original and everted states corresponding to steps

1 and 2 in Fig. 4, whereas *snap-back* occurs when the system in its everted state returns to its original shape corresponding to steps 3 and 4 in Fig. 4. Elastic instabilities of this type occur upon the application of a compressive loading and can be triggered by numerous factors (e.g. geometry or material properties, see e.g. [34]).

The first set of computational experiments conducted in this work was the stability study carried out with the goal of identifying the mono- and bistable dome shell configurations for different geometrical parameters. One typical computation of the stability study consists of two steps as sketched in Fig. 4: first, a vertical displacement is applied at the top of the dome along the direction opposite to the y axis (step 1 in Fig. 4). The magnitude of the applied displacement must be sufficiently high to trigger the instability. Secondly, the system is let to relax (step 2 in Fig. 4). No displacement is applied in this step. During this computation, dome shells are deformed from the original state to the everted state, then they remain in their everted shape if bistable, whereas they relax back to original shape if monostable.

To discriminate between bistable and monostable configurations, the computed strain energy was analyzed. A stable equilibrium state corresponds to a strain energy local minimum. Hence, a bistable configuration is a configuration that presents two minima in its strain energy landscape (two stable equilibria). To investigate the embedded dome shell stability, the strain energy U (here the total strain energy of the numerical model, ALLSE in Abaqus) was computed at each displacement $\underline{x}$ increment during the loading step and the minimum criteria were analyzed following the protocol used in prior studies [2]. These read:

$$\frac{\partial U}{\partial \underline{x}} = 0 \tag{4}$$

$$\frac{\partial^2 U}{\partial \underline{x}^2} > 0 \tag{5}$$

For a deformed dome shell, a strain energy minimum can be identified when Eqs. (4) and (5) are satisfied at the same displacement $\underline{x}$ increment. The case where only Eq. (4) is satisfied corresponds to a local strain energy maximum *i.e.* an unstable equilibrium. Quadratic hexahedral hybrid volumic elements with reduced integration C3D20RH have been used to mesh the dome shell geometries for the stability study. It is noted in passing that three-dimensional four-node shell elements (S4R) could not be used to mesh the dome shell as the hyperelastic Neo-Hookean model could not be implemented with this type of elements. To overcome hourglass issues associated with reduced integration elements, hourglass control was set to *enhanced* during the computation. The number of elements has been determined through a convergence analysis. The latter was found to vary with the dome half-angle α, where increasing α requires an increasing number of elements. For shallow domes, around 18k elements were used, whereas, deeper domes require around 23k elements.

2.4.2. Strain energy asymmetry analysis

The second set of computational experiments conducted in this work was the strain energy asymmetry study carried out with the goal of quantifying which combinations of dome shell geometrical parameters lead to a highly asymmetric strain energy required for snap-back. The quantification of such a asymmetric transition between the two stable states can in turn provide novel geometric design rules for creating morphing structures with programmable shape switch and strategy. A recent example where asymmetric bistable systems are employed is provided in Ref. [47]. The energy asymmetry study was carried out only for bistable dome shell geometries identified by the stability analysis (Section 2.4.1). It consists of two steps as illustrated in Fig. 4: a loading step with a positive vertical displacement is first applied onto the top of the dome shell (step 3 in Fig. 4). This is followed by a recovery step (step 4 in Fig. 4) during which the system is let to relax. During this computation, dome shells are deformed from the everted state to the original one. For these computational experiments linear
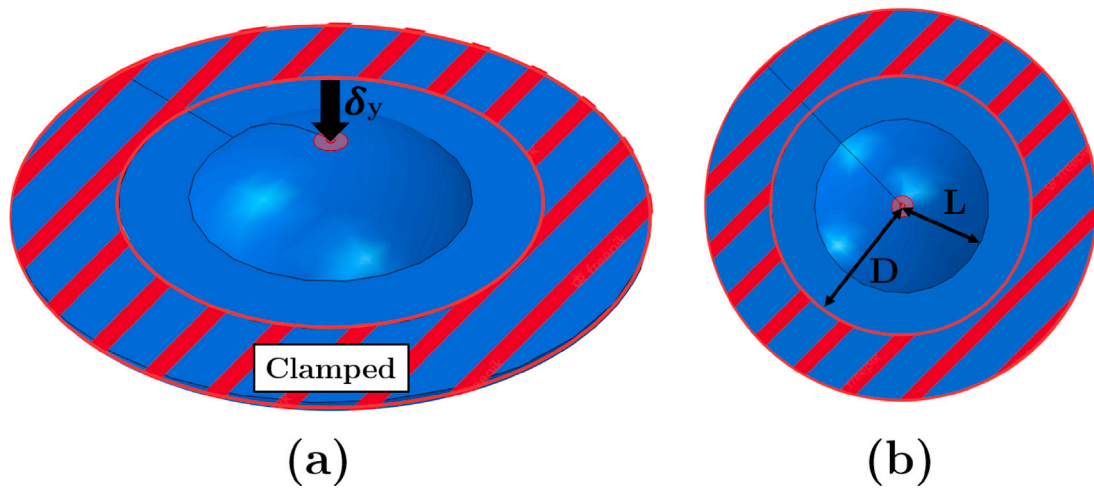
Fig. 3. FE boundary conditions and loading of the geometrical dome shell model used throughout the computational experiments. (a) Isometric view showing the loading modeled by imposing a vertical displacement δ_y at the top of the dome together with the clamped BCs applied at shell's outer edge ; (b) top view of the geometrical model illustrating the definition of the clamping distance D and the lateral size of the dome L.
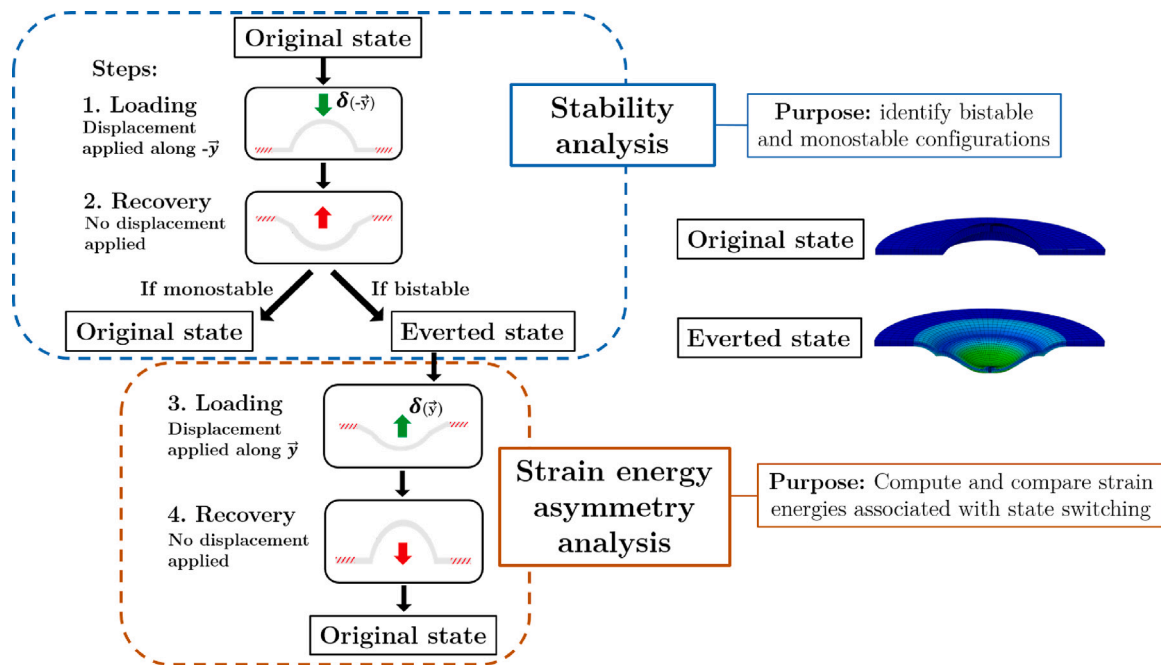

Fig. 4. Flow chart representing the steps during computational experiments: first, the stability analysis allows to identify monostable and bistable configurations (steps 1 and 2), and then the asymmetry analysis allows to compute the strain energy required for state switching (steps 3 and 4). Each analysis requires one loading step and one recovery step.

hexahedral hybrid volumic elements (C3D8RH) have been used in order to minimize the computational time. The number of elements used to ensure convergence of the results as well as the hourglass control strategy are detailed in Section 2.4.1.

2.5. Experimental methods

To validate the results of the FE simulations, the mechanical behavior of the embedded dome shells was investigated experimentally for selected dome geometries. Experiments were conducted onto $3D$-printed test samples that were subjected to a compressive loading applied by means of dead loads. The sample manufacturing and experimental protocol are described hereinafter.

2.5.1. Experimental sample manufacturing

Test samples have been 3D-printed using a Stratasys EDEN 260 VS 3D-printer using TangoBlack FLX 930 resin. This 3D-printer uses a Polyjet technology where micrometric sized droplets with resolution of ca. 16 μm of liquid photopolymer are deposited layer by layer onto a build tray and cured instantly under UV light [61–63]. The PolyJet technology was selected for its high-accuracy of the $3D$-printed parts as shown by earlier studies on structures with complex geometry [8, 56,62,63].

From the computational experiments, two bistable configurations have been chosen for manufacturing and experiments. Notably, test samples with two selected combinations of the inner radius R and half-angle α were selected and $3D$-printed, namely ($R = 15$ $mm, \alpha = 45°$) and ($R = 20$ $mm, \alpha = 40°$). Samples are presented in Fig. 5(a). Each of these two configurations has been printed with the same thickness $h = 0.5$ mm. As seen, a small hole of radius 2 mm has been manufactured at the top of the dome samples in order to apply experimentally the compressive load (see Section 2.5.2). Consequently, the numerical models of the dome shell geometry used for comparison with experiments
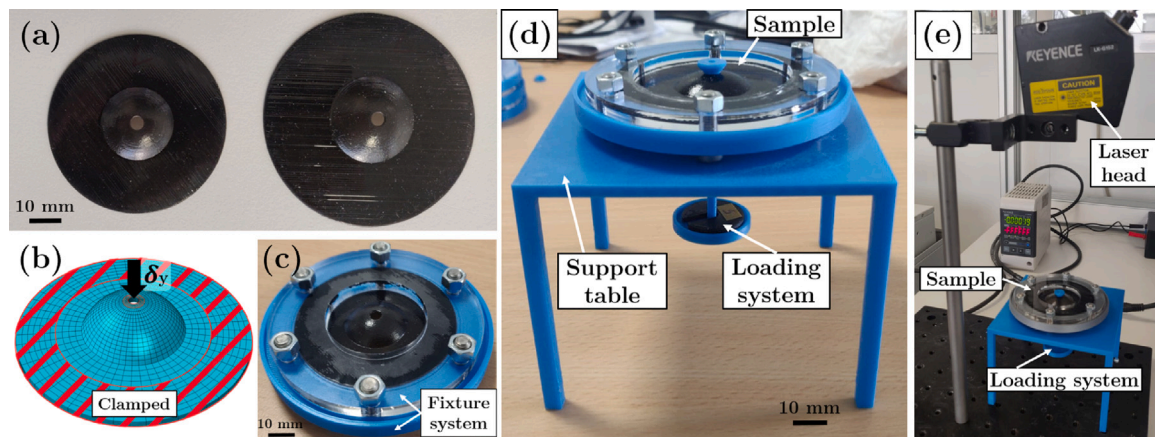
Fig. 5. (a) $3D$-printed test samples with ($R = 15$ mm, $\alpha = 45°$) at left and ($R = 20$ mm, $\alpha = 40°$) at right. Both samples have equal thickness $h = 0.5$ mm ; (b) FE-equivalent geometrical model with applied BCs and vertical displacement δ_y applied at the top of the dome to simulate the compressive force in experiments ; (c) a fixture system that encloses the test sample by means of a series of bolts. (d)–(e) Testing set-up used to study the mechanical behavior of selected dome shell geometries. It consists of (d) a loading system that allows to apply dead-load weights on the sample, laying on the support table. The displacement is recorded via a laser-head shown in (e).

were also designed to contain the small hole at the top of the dome, see Fig. 5(b).

2.5.2. Experimental set-up and protocol

A novel experimental testing set-up is proposed in this work to measure the load–displacement response of dome shell structures. It is presented in Fig. 5(e) and comprised several parts that were fabricated using Fused-Deposition-Modeling (FDM) 3D-printing technology. The experimental set-up was designed to reproduce faithfully the clamped BCs used for computational experiments (see Figs. 5(b), (c)). The fixture system is composed of two plates bolted together and encloses the test samples (see Fig. 5(c)). The friction resulting from the bolting system allows to reproduce the clamped BCs. The top plate of the fixture system is made of transparent polymer (thermoplastic PMMA with materials properties $E = 3.0$ GPa ; $\nu = 0.37$) chosen to allow the centering of the sample. This was achieved with the help of a groove manufactured into the polymeric bottom plate (made of thermoplastic ABS with material properties $E = 1.5$ GPa ; $\nu = 0.3$). The fixture system enclosing the sample is laying on a support table in order to allow the application of the compressive force via dead loads, see Fig. 5(d). In previous work [64,65], dead loads have been successfully used in order to trigger elastic instability in soft structures. To apply the compressive force, the loading system is composed of a rod and plates assembly (made of ABS) on which weights can be stacked (see Fig. 5(d) with the rod and plates in blue and weights in black). Weights have been manufactured using FDM 3D-printing in the form of thick disks, whereby changing the thickness allowed to attain different masses. To measure the vertical displacement a laser head (Keyence LK-G152) was used with displacement accuracy below 1 μm. The laser head is placed at a certain distance from the testing set-up in order to record the displacement of the rod top part from above, see Fig. 5(e). To ease the measurements, the rod was designed to contain a small circular plate at its top see Figs. 5(d), (e). The latter serves as contact surface with the top of the dome, as well as mirror surface for the laser head.

Experiments were carried out following the protocol described hereinafter. First, the sample is placed inside the fixture system and is carefully centered. The assembly is then put on the support table under the laser head, and the loading system is inserted through the sample's hole. The laser head is set to zero. After the installation steps, weights are incrementally added to the loading system until the snapping occurs. For each added weights, the displacement is recorded. After snapping, all the weights are removed to record the position of the second stable state. It is, however, important to note that as the loading system itself has a mass, the exact position of the first and second stable state cannot be measured directly using the current set-up. The initial

and final measured positions are therefore offset with the displacement corresponding to the loading system mass. Each experiment is repeated four times to ensure repeatable measurements, whereby only the order of the applied weights is changed in order to get as close as possible to the onset of instability.

3. Results and discussion

In this section, the results of both experiments and simulations for the mechanical response of embedded dome shells are presented and discussed. It consists of three subsections. Specifically, the results of the parametric numerical stability analysis of embedded dome shells are first presented in Section 3.1 and the load–displacement response for selected dome geometries are compared with the results of experiments in Section 3.2. Finally, the results of the strain energy asymmetry analysis are reported in Section 3.3, whereby an index is proposed to quantify the *energy barrier* asymmetry, which constitutes the novelty of this work.

3.1. Dome shell structures stability

This subsection is organized as follows. First, the salient features of a representative embedded dome shell structure are discussed (Section 3.1.1), whereas the mono- and bistable domains resulting from the parametric study are given in Section 3.1.2.

3.1.1. Computational investigation of the bistability of an embedded dome shell

The load–displacement and corresponding strain energy U curves, computed using the numerical framework described in Section 2.3, are reported in Fig. 6(a) for a representative bistable dome geometry. The latter is defined by the following geometrical parameters: inner radius $R = 10$ mm, dome half-angle $\alpha = 52°$ and thickness $h = 1$ mm. Fig. 6(a) represents the transition from the *original* to the *everted* state, which in turn corresponds to the dome shell *snap-though* behavior. In Fig. 6(a) the load–displacement curve is depicted in black color, whereby a solid and a dotted lines are used respectively to indicate the loading (from ① to ④) and the recovery step (from ④ to ⑤). The strain energy is instead reported in red color. To provide an exhaustive description of the bistability dome shell features, the different deformation profiles for the dome bottom edge are extracted from the FE results at discrete deformation steps, and are reported in Fig. 6(b). Likewise, isometric views of the dome half-section extracted from the computations are given in Fig. 6(c) to enrich the discussion.
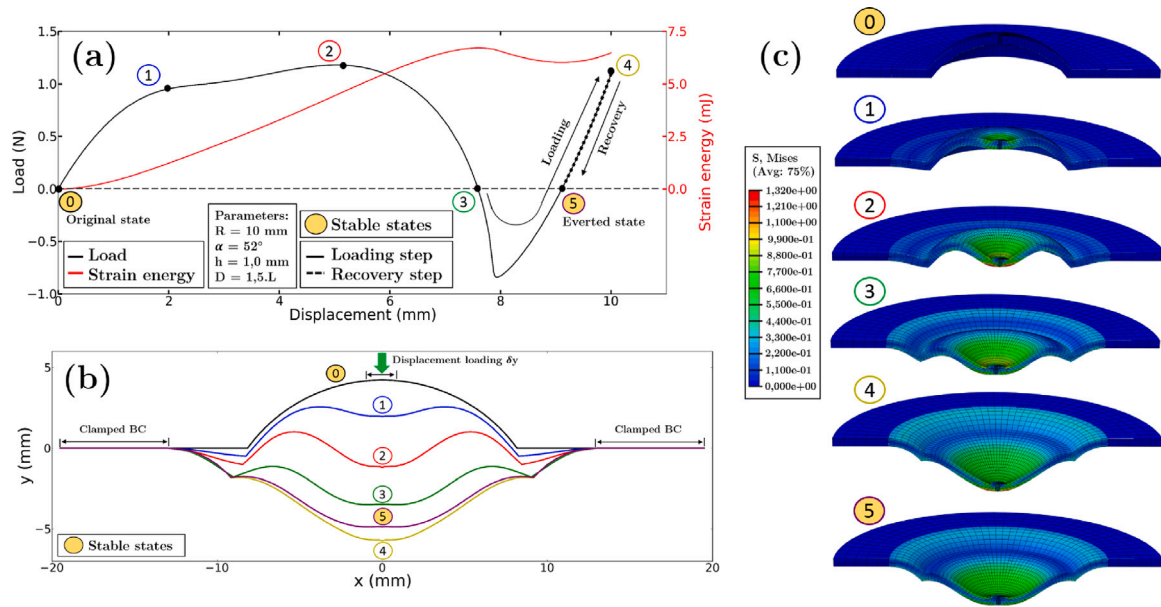
Fig. 6. Numerical response of a representative bistable dome shell geometry with inner radius $R = 10$ mm, dome half-angle $\alpha = 52°$ and thickness $h = 1$ mm. (a) Representative load–displacement and strain energy curves during stable states transition and corresponding deformation profiles of the dome (b) bottom edge and (c) half-section at discrete deformation steps.

Different deformation stages can be observed during the transition from the first to the second stable state. The first stage ⓪ corresponds to the first stable state of the dome and is considered to be stress free. As the load increases, the plate and the dome begin to buckle (stage ①) and undergo large deformations until the peak load is reached (stage ②). As seen in Figs. 6(b), (c) the corresponding deformed shapes of the dome exhibit a wave-like geometry with deformation localized at the dome top. Past this point, the load starts decreasing until it changes sign. The third stage ③ thus represents the onset of instability and is also an unstable equilibrium point with $\frac{\partial U}{\partial x} = 0$). Past this stage, the dome does not need any additional loading to reach the second stable state. As the displacement continues to increase, the dome shape is in its *everted* state (see Figs. 6(b), (c)), and the load increases again until the end of the loading step (stage ④). The recovery step lets the system relax without any applied displacement, and reaches the second stable state (stage ⑤). This point corresponds to a strain energy well that fulfills both stability conditions (see Section 2.4). Moreover, since the second stable state is a strain energy equilibrium point with $U \neq 0$, this point is consequently not stress-free. This observation is corroborated by Figs. 6(b), (c) at stage ⑤. Interestingly, one can observe the *everted* shape of the dome is not faithfully correspondent to the *original* one. Examples of load–displacement curves for dome geometries corresponding to $R = 10$ mm, $h = 1$ mm and varying dome half-angle α are reported in Fig. 7. These parameters lead to dome shell structures that are either monostable and bistable. Load–displacement curves are depicted using respectively a solid line for the transition from the original state to the everted state (snap-through) and dotted line for the transition from the everted state to the original state (snap-back). Likewise step ⓪ and step ⑤ correspond to the two equilibrium state, i.e. *original* and *everted*. Displacements have been normalized by dome heights H so that all plots can be displayed in the same graph, and different colors correspond to different values of the half angle α value, all else equal.

From Fig. 7, one is able to discriminate dome that exhibit a monostable response (black curve) from those whose response is bistable (color curves). Notably, the system becomes bistable with the increase of α and notably for $\alpha \geq 42°$ (colored lines). Moreover, the load peak also increases with increasing α, the deeper the shell the higher the load peak. Interestingly, by varying α the load–displacement curve for the loading and relaxation step is not the same. A difference is observed

for $\alpha \geq 55°$. It is expected that this change of path influences the *energy barrier* asymmetry, as it is discussed in Section 3.3.

3.1.2. Stability domains

Results of the parametric stability analysis conducted for dome shell geometries with values of the parameters given in Table 1 are reported hereinafter. Following the numerical protocol described in Section 2.4.1, stability domains were identified numerically. It is noted in passing that around 50 computations have been conducted to this purpose. Results are summarized in Fig. 8, whereby bistable and monostable region correspond to the blue and light red areas. Specifically, data are reported as a function of the dome inner radius R and half-angle α, whereas the thickness h was increased from $h = 0.5$ to $h = 1$ mm. As seen, the thickness of the shell h shifts the border between the two domains, and it is highlighted with shaded blue color. Equally important, one can observe that changing the distance D to the clamped BCs also varies the domain boundaries. Specifically, increasing D decreases the bistable domain, which implies that the clamping BCs influences the ratio of stretching to bending energy of the dome shell in agreement with earlier work [45].

Collectively, data reported in Fig. 8 are consistent with prior studies [40,41,45]. Notably, they show that the bistable domain increases with the increase of dome radius R and half-angle α. It is noteworthy to observe that, in the present study, values of the dome thickness above $h = 1$ mm were not explored. Prior work [40,41] shows that past this value the bistability domain decreases.

3.2. Experimental results

Prior to presenting the experimental results and their comparison with the simulations, it is worth mentioning that, although several test samples were 3D-printed with different geometrical parameters, only two geometric configurations could be exploitable for experiments (see 5(a)). The other samples prematurely broke during manipulation, very likely due to a severe strain localization exceeding the strain at failure of the constituent polymer. To overcome the issue with the limited number of available samples for experiments, we opted to design and to fabricate another fixture system that enabled the same geometry to be tested under different BCs, namely with different clamping distances D.
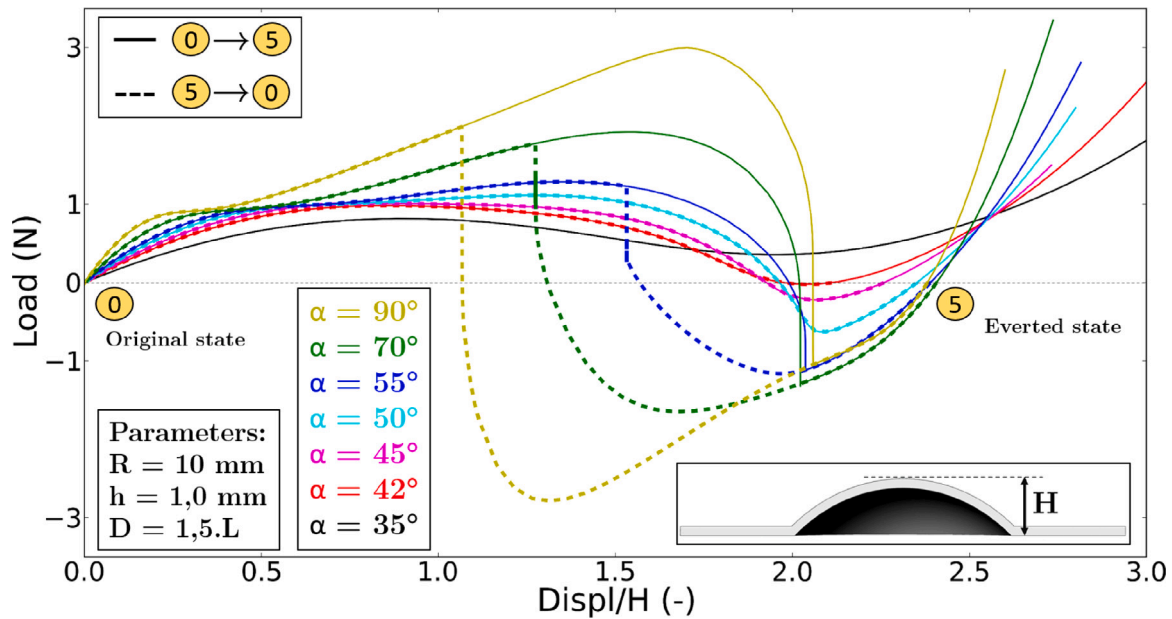
Fig. 7. Numerical response of dome shells with inner radius $R = 10$ mm, thickness $h = 1$ mm and varying half-angle $\alpha = 52°$. These geometries correspond to structures with either a monostable (black curve) or bistable response (color curves). Solid lines correspond to load path from original to everted stable state. Dotted lines correspond to the reversed load path, from everted to original stable state.
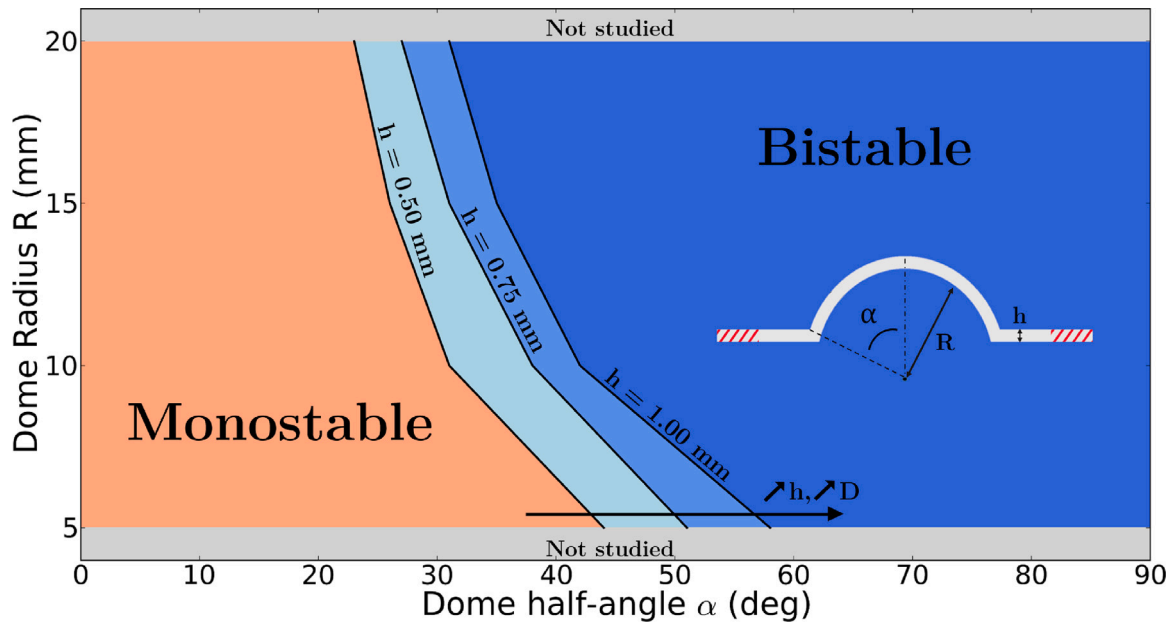

Fig. 8. FE identified stability domains of embedded dome shells: monostable (in light red) and bistable (in blue shades) domains for different thicknesses h (0.5, 0.75 and 1 mm) depending on dome radius R and dome half-angle α, with fixed parameter $D = 1.5 * L$. The definition of all geometric parameters is recalled in the right part of the figure.

Specifically, two different distances have been considered : $D/L = 1.5$ and $D/L = 2.0$ and the resulting load–displacement curves measured experimentally are reported in Fig. 9. Since the load was applied by means of dead loads, the reported experimental curves are discrete. As explained in Section 3.2, for each sample geometry and BCs, the experiments were repeated four times and different color were used to report the measured data (Fig. 9). In the interest of comparison, the results of the FE simulations for the corresponding numerical dome geometries are also reported (black solid lines in Fig. 9).

Collectively, data in Fig. 9 show a good agreement between experiments and simulations, in turn confirming the robustness of our numerical methods. Notably, the load–displacement is observed to increase monotonically until the onset of instability, which is a precursor

of the elastic *snap-through*. Moreover, one can see that the experimental points recorded after snapping are very close to FE results and that the experimental unloading lies close to the FE curve. Interestingly, the comparison between the load and displacement values at which snapping occurs is also highly satisfactory. In the computations, the latter corresponds to the point at which the load starts decreasing (x symbol in Fig. 9), whereas in experiments it corresponds to the maximum load. On the other hand, one can see that the attainment of maximum load – followed by a rapid load decrease – observed in the FE computations could not be captured in experiments. The reason for this is simple. Since the loading system can only add incrementally the weights (i.e. dead loads), the experimental force cannot decrease.
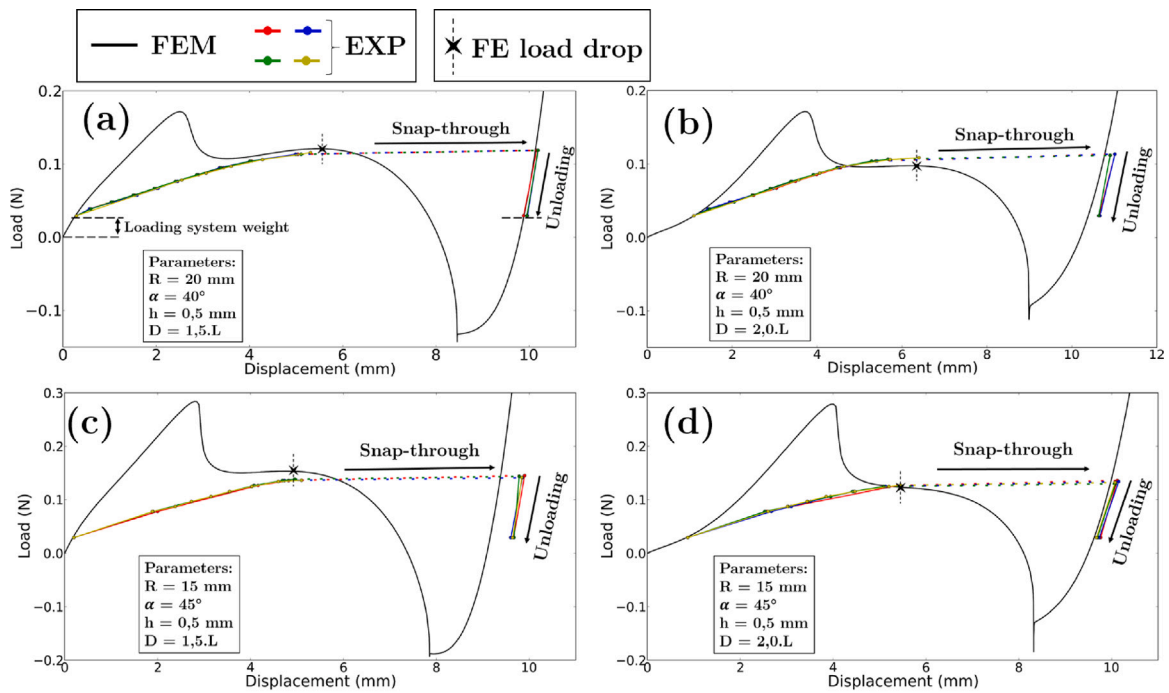
Fig. 9. Comparison between FEM (black line) and experimental (colored line) load–displacement curves for two geometric dome shell configurations and two clamping distances (i.e. $D = 1.5*L$ in (a), (c) and $D = 2.0*L$ in (b), (d).

Therefore, unlike the simulations, the experimental curves exhibit snap-through behavior at peak load. Equally important, the absence of a sharp maximum load in experiments can be rationalized by the way the load is applied at the top of the dome. Such first load peak has also been reported in experimental studies of thin domes [38] and in bistable woven domes [66]. To investigate the influence of the finite-size area on which the displacement is applied, additional FE computations were carried out for different values of this parameter. The results (reported in Appendix) show that the larger the surface of applied displacement, the higher the load peak. Finally, comparing pairwise Figs. 9 (a), (b) and Figs. 9 (b), (c) highlights the influence of the distance D to the clamped BCs. As seen, increasing the distance delays the onset of instability (i.e. the intersection with the zero load line) and also increases the distance between the first and the second stable state. Load levels are instead slightly affected, with lower values at load drop in the case of the higher distance (Figs. 9 (b), (d)).

3.3. Asymmetric bistability of embedded dome shells

The results of the computational experiments carried out onto bistable dome shells with the goal of quantifying the so-called *energy strength* [52] for *snap-back* (Section 2.4.2) are presented below. In the interest of clarity, these results are presented using a simple *asymmetry index*, designated as τ. This is defined as followed, e.g.

$$\tau = \frac{U_{1\to2} - U_{2\to1}}{U_{1\to2}} \tag{6}$$

In Eq. (6), $U_{1\to2}$ designates the strain energy necessary to switch from the original *as manufactured* state to the *everted*. The former is referred to as state 1 in Fig. 10(left) or as stage ⓪ in Fig. 6), whereas the latter as state 2 in Fig. 10(left), or stage ⑤ in Fig. 6. Likewise, $U_{1\to2}$ designates the strain energy necessary to *snap-back* from the *everted* to the *original* state. For embedded bistable dome shells, $U_{1\to2}$ is always strictly superior to $U_{2\to1}$ ($U_{1\to2} > U_{2\to1}$). In other words, the *strength* of stability of the original state is always superior to the strength of stability of the everted state. The index τ is therefore constraint between 1 (high asymmetry, i.e. $U_{1\to2} \gg U_{2\to1}$) and 0 (low asymmetry, or equality, i.e. $U_{1\to2} = U_{2\to1}$). Results of the FE strain energy asymmetry analysis

for bistable dome shell geometries are reported in Fig. 10(right). In the interest of clarity, selected results corresponding to dome geometries with $R = 10$ mm, $h = 1$ mm and $D = 1.5*L$ and α comprised between 42 ° and 90 ° are given.

Collectively, data show that the higher is the dome half angle α, the lower is the asymmetry. Moreover, this plot can be broken down into two separate parts, namely a high asymmetry part denoted A (encircled with an orange dotted line), and a low asymmetry part denoted B (encircled with a green dotted line). It can be noted that at the bistability limit ($\alpha = 42°$ in the case of this dome shell geometry, see Fig. 9), τ is nearly equal to 1. The passage from A to B is abrupt, and occurs in the case described in Fig. 10 between $\alpha = 53°$ and 54°. To rationalize the origin of the abrupt drop from A to B, the FE load–displacement curves corresponding to $\alpha = 45°$ and $\alpha = 70°$ are reported in Fig. 11(a). The dome with lowest α (i.e. $\alpha = 45°$), called *shallow* shell, exhibits a load–displacement curve that is the same when going from state 1 to state 2 and vice versa. Consequently, both curves intersect the zero load line at the same absolute position. This intersection with the displacement axis corresponds to the stability state transition point. However, the displacement from the stable state 2 to the transition point being largely smaller than from the stable state 1 to the transition point, the energy needed $U_{2\to1}$ is therefore much lower than $U_{1\to2}$, explaining the high asymmetry. Unlike what observed for the shallow dome, the dome corresponding to $\alpha = 70°$, called *deep* shell, presents a low asymmetry. The load–displacement path from stable state 1 to stable state 2 is not the same than that from stable state 2 to stable state 1, as shown in Fig. 11(a). Consequently, the intersection between the displacement axis and the load–displacement curve is different, as can be seen on Fig. 11. The distance between the two stability state transition points, denoted Δ, is thus non-null. It is in turn reasonable to expect that as the distance from stable state 2 to the state transition point increases, the strain energy $U_{2\to1}$ increases correspondingly and the asymmetry decreases. Shells exhibiting this behavior therefore are likely to present low asymmetry. To provide evidence, Fig. 11(b) reports the evolution of Δ as a function of the dome half angle α for all dome geometries studied in Fig. 10. The results Fig. 11(b) confirm that, for all shallow dome shell geometries
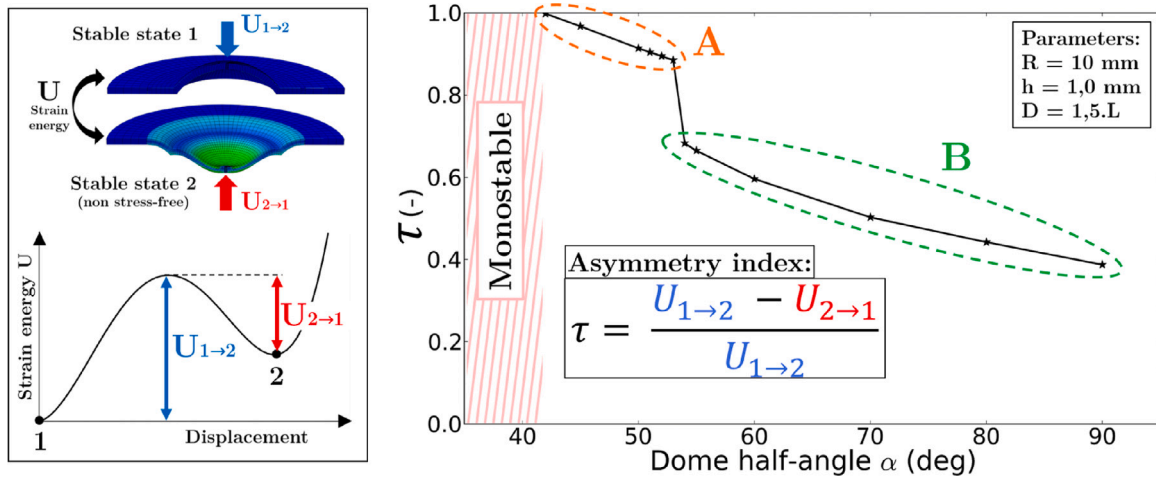
Fig. 10. (left) Definition of the strain energies necessary to switch between the first (original) and the second (everted) stable states. Specifically, $U_{1\to2}$ corresponds to the strain energy associated with the transition from state 1 to state 2 (in blue), whereas $U_{2\to1}$ corresponds to the opposite transition (in red). (right) Definition of the asymmetry index τ and its corresponded values computed by means of FE simulations for a specific geometric configuration with varying α. Two distinct parts with high (A in orange) and low (B in green) asymmetry can be observed.
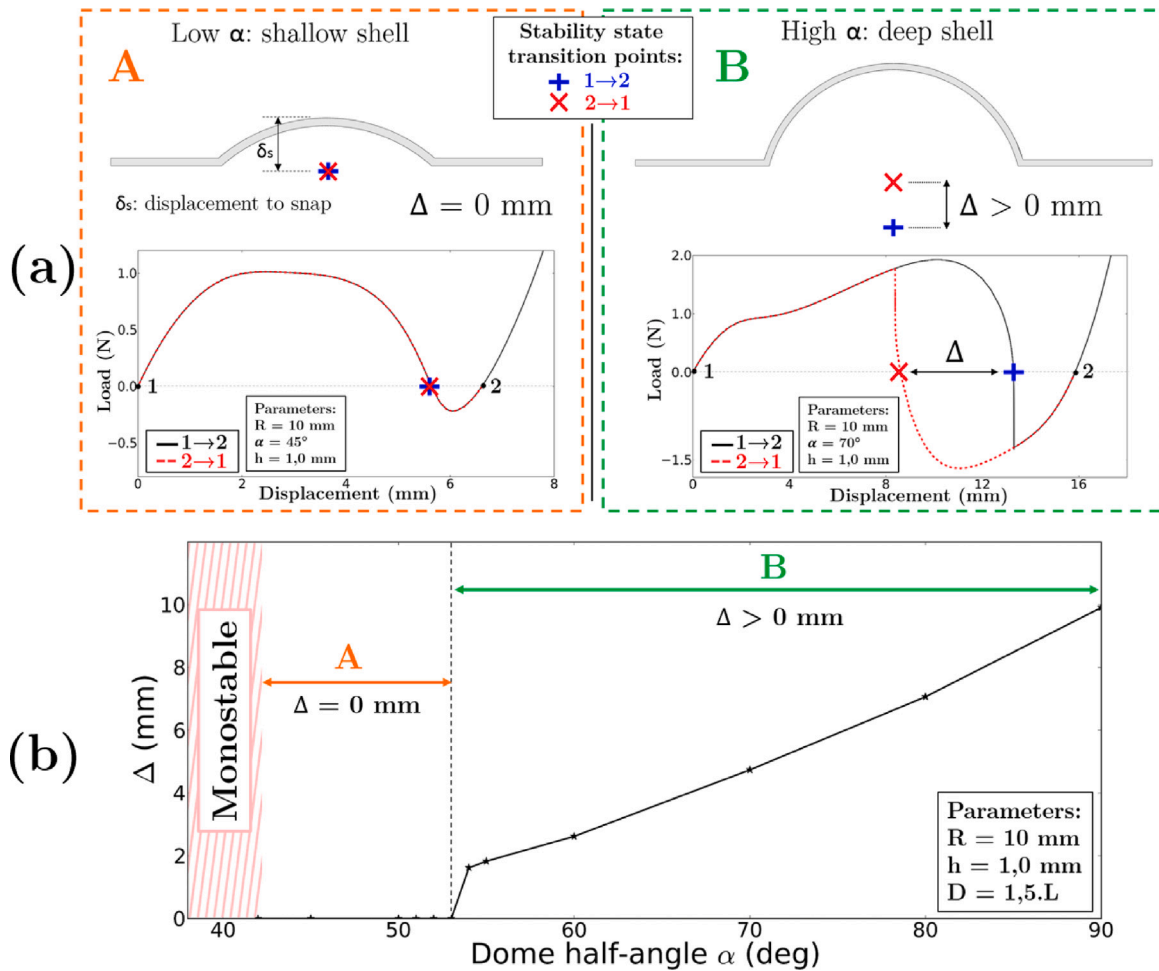

Fig. 11. (a) Load–displacement curves for two dome shell geometries characterized by a low $\alpha = 45°$ (A in orange) and a high $\alpha = 70°$ (B in green), all else equal. The stability transition points are defined with red and blue symbols and correspond to the minimum displacement necessary to trigger the snapping from one stable state to another. The distance between these two points is denoted as Δ. (b) Evolution of the distance Δ between stability state transition points as a function of the deepness of the shell. Δ has a positive finite magnitude for deep shells ($\alpha > 53°$, in green), whereas it is equal to zero for shallow shells ($\alpha \leq 53°$, in orange).

(i.e. $\alpha \leq 53°$), $\Delta = 0$ mm. This distance abruptly rises when $\alpha > 53°$ as the deepness of the shell increases, entering the realm of deep shells.

Δ grows quickly with the increase of α, explaining the reduction of the asymmetry index τ with α.

Finally, to provide an exhaustive roadmap for the design of bistable embedded dome shells with tunable *energy barrier asymmetry* the asymmetry index τ for all geometries explored in this study (see Table 1) is reported in Fig. 12. For the sake of comparison, data are reported as a function of both the dimensionless dome geometric parameter λ defined in Eq. (1) (see Fig. 12(a)) and of distance Δ between the transition points (see Fig. 12(b)). Collectively, data show similar trends. Notably, all computed values of τ collapse in one curve and a clear separation into the region of *high* and *low asymmetry* is observed. Specifically, the high asymmetry region contains asymmetry indexes τ between 0.99 and 0.86, whereas τ varies between 0.69 and 0.25 in the low asymmetry region. No computed asymmetry indexes was found between the extreme values of those two parts. As Fig. 12 highlights, the dimensionless energetic parameter τ proves an effective simple parameter to quantify the asymmetric nature of bistability of dome shells. Equally important, it can be nicely expressed as a function of the dimensionless parameter λ that is widely employed in studies of dome structures [38,39]. Therefore, the results in Fig. 12(a) provide simple guidelines for the design of bistable dome shells. For example, if a high asymmetric bistable system is sought, its geometry should be chosen to be described by λ between 4 and 5.5. Vice versa, to design highly symmetric bistable systems, λ must be chosen as high as possible.

The origin of *energy strength asymmetry* is two-fold. One relies on geometry and imperfection sensitivity in agreement with recent studies on spherical shells [67] and slender beams [8]. The other can be explained on account of the fact that the everted state is not stress-free as part of the strain energy is stored (see Fig. 10(left)). While this energy landscape asymmetry has already been observed for bistable valves that switch stable states for different pressure thresholds [47] or for rotational bistable structures [68], its quantification is reported here for the first time. Interestingly, it is noted in passing that asymmetry can be obtained starting from symmetric systems. For example, Danish et al. [69] obtained tailorable asymmetric energy landscape by attaching a composite strip to a square bistable cross-ply laminate (which displays symmetric behavior), whereas Wang et al. achieved tunable asymmetry for bistable energy harvester [70].

4. Conclusions and perspectives

In this work, the mechanical behavior of embedded dome shell structures was studied by means of both FE simulations and experiments. The computations were carried out in a finite-strain setting and stability was investigated for a variety of geometrical parameters, whereas clamped BCs were used throughout the computational study. Two sets of computations were conducted using the Static Damping Method. The stability of dome systems was studied first, and the results for a representative geometry were presented and analyzed. They showed that the onset of *snap-through instability* occurs when the load becomes equal to zero and that the *everted* dome shape extracted form FE simulations is not stress-free. Moreover, the latter is shown to differ from the *original, i.e. as manufactured* dome shape. The geometrical parameters of the dome (i.e its inner radius R, thickness h and half-angle α) were then varied systematically in order to identify the mono- and bistable domains. Specifically, our results showed that the bistable domain increases with the increase of dome radius R and half-angle α in agreement with prior studies. To validate the numerical results, experiments were then conducted onto 3D-printed test samples of selected dome geometries and a dedicated set-up was designed and fabricated to measure their load–displacement response. The agreement proved very satisfactory, with the main difference being the occurrence of snap-through instability in correspondence of the maximum load in the experimental load–displacement curve. Given the robustness of the numerical methods, the strain energy landscape for bistable dome shells was then studied by means of computations. Results showed that, for specific combinations of the dome geometrical parameters, the strain energy required to switch from the original stable state to the everted

stable state is larger than that required for the opposite transition to occur. This observation shows evidence of a *energy strength asymmetry* in the dome shell behavior. The mechanisms underlying the asymmetry were investigated and an asymmetry index τ was proposed. The index was calculated for numerous dome shell geometric parameters showing that shallow shells ($4.0 < \lambda < 5.5$) exhibit high asymmetry, whereas deep shells ($\lambda > 5.2$) do not. This result was rationalized on account of the load–displacement path exhibited by the dome upon loading and unloading. The latter was shown to be identical for shallow dome shells, which then require a lower strain energy upon unloading. Collectively, the results of this work can be used as a design guideline for the conception of smart multistable systems that harness the tunable bistability of embedded dome shells.

Declaration of competing interest

Data availability

Data will be made available on request.

Appendix. Comparison between FE and experimental results

It has been seen that experimental load–displacement curves differ from FE computed results. This section proposes explanations for the observed differences.

The experimental loading system is composed of 2 parts, one of them being in contact with the top of the dome (see Fig. 5(d)) through a ring-shaped flat surface. This contact is used to apply the displacement. However, the real contact surface between the dome and the part is unknown although it has an important influence on the shape of the FE load–displacement curve. Fig. A.13 presents the comparison of 3 different contact surfaces, their influence on FE results, and is compared with corresponding experimental curves for one geometric configuration.

The ring-shaped contact surface can be described by its inner radius R_i and its outer radius R_e. By design, R_i is equal to the dome hole radius: 2 mm. Three cases have been numerically explored in Fig. A.13, corresponding to three contact surface sizes: small size ($R_e = 2.1$ mm, thin black line), medium size ($R_e = 2.5$ mm, medium black line) and the large size ($R_e = 3.0$ mm, thick black line) that corresponds to the size of the loading system part flat surface. It can be seen that the contact
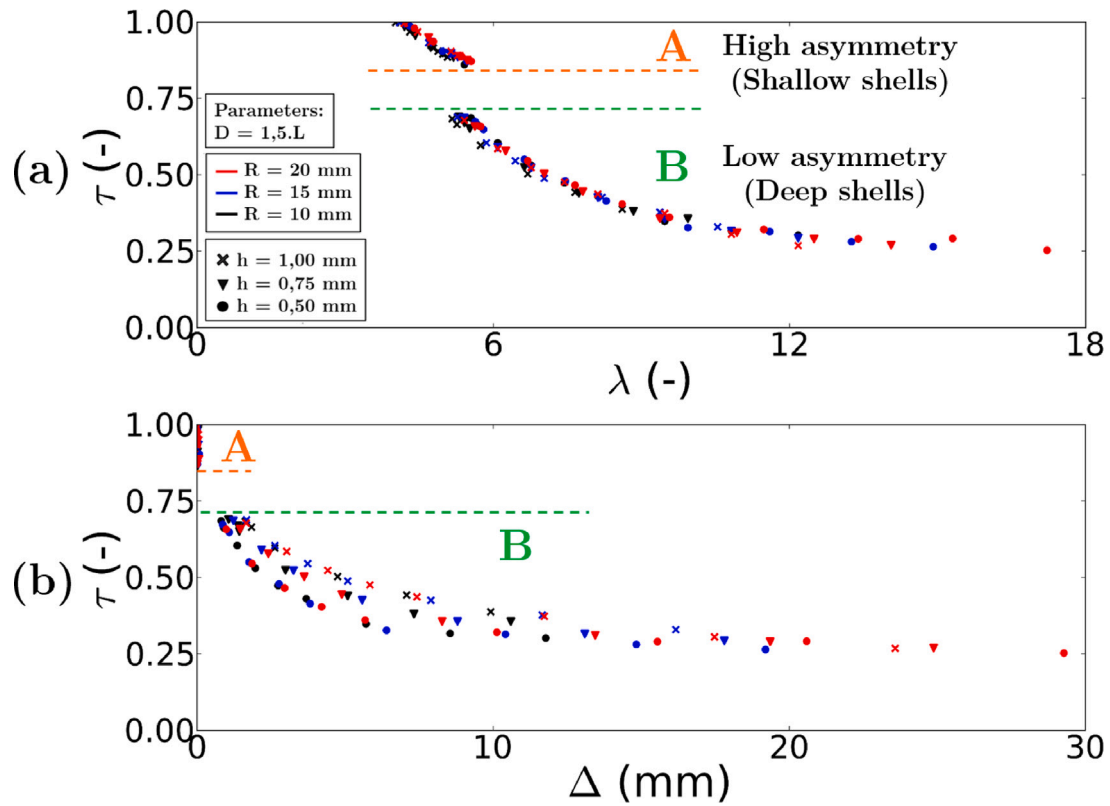
Fig. 12. Strain energy asymmetry index τ for different embedded dome shell parameters R, h and fixed parameter $D = 1.5*L$ as a function of the dimensionless dome geometric parameter λ (a) and of distance Δ between the transition points (b). Shallow shells present high asymmetry index (τ between 0.99 and 0.86, above the orange line), while deep shells present lower asymmetry index (τ between 0.69 and 0.25, below the green line).
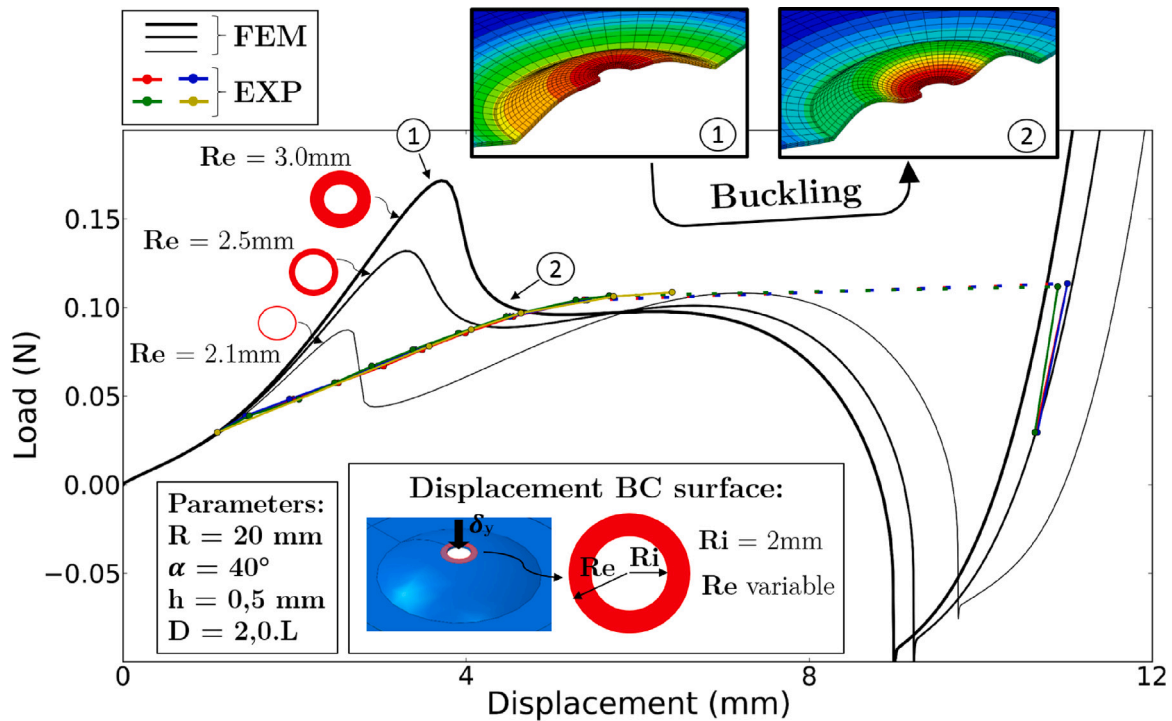

Fig. A.13. FE load–displacement curves for different sizes of the applied displacement surface, and comparison with experimental results; definition of the displacement surface corresponding to experimental conditions, and depiction of dome buckling that corresponds to the observed FE load peak.

size has an important influence on the shape of FE curves, particularly on the load peak, the displacement at load drop and even the position of the second stable state. The largest surface induces the highest load peak, that corresponds to the buckling of the top of the dome. The smallest surface shows a lower initial peak, and the corresponding curve has a shape similar to those of dome shell without hole. The

load drop of the smallest surface is close to the experimental peak load. Increasing the surface also has the effect of decreasing the displacement at load drop, and consequently the position of the second stable state.

It is expected that the actual contact surface changes as the dome shell deforms under the applied displacement. A way to improve the FE modeling could be therefore to use contact analysis using CAD geometries of both sample and loading system part.

References

[1] Kochmann DM, Bertoldi K. Exploiting microstructural instabilities in solids and structures: From metamaterials to structural transitions. Appl Mech Rev 2017;69(5). http://dx.doi.org/10.1115/1.4037966.

[2] Mofatteh H, Shahryari B, Mirabolghasemi A, Seyedkanani A, Shirzadkhani R, Desharnais G, et al. Programming multistable metamaterials to discover latent functionalities. Adv Sci 2022;9(33):2202883. http://dx.doi.org/10.1002/advs.202202883.

[3] Cao Y, Derakhshani M, Fang Y, Huang G, Cao C. Bistable structures for advanced functional systems. Adv Funct Mater 2021;31(45):2106231. http://dx.doi.org/10.1002/adfm.202106231.

[4] Platus DL. Negative-stiffness-mechanism vibration isolation systems. In: Vibration control in microelectronics, optics, and metrology, vol. 1619. SPIE; 1992, p. 44–54. http://dx.doi.org/10.1117/12.56823.

[5] Wang YC, Lakes RS. Extreme stiffness systems due to negative stiffness elements. Amer J Phys 2004;72(1):40–50. http://dx.doi.org/10.1119/1.1619140.

[6] Fritzen F, Kochmann DM. Material instability-induced extreme damping in composites: A computational study. Int J Solids Struct 2014;51(23–24):4101–12.

[7] Bertoldi K, Boyce MC. Wave propagation and instabilities in monolithic and periodically structured elastomeric materials undergoing large deformations. Phys Rev B 2008;78(18):184107. http://dx.doi.org/10.1103/PhysRevB.78.184107, Publisher: American Physical Society.

[8] Tarantino MG, Danas K. Programmable higher-order Euler buckling modes in hierarchical beams. Int J Solids Struct 2019;167:170–83. http://dx.doi.org/10.1016/j.ijsolstr.2019.03.009.

[9] Holmes DP. Elasticity and stability of shape-shifting structures. Curr Opinion Colloid Interface Sci 2019;40:118–37. http://dx.doi.org/10.1016/j.cocis.2019.02.008.

[10] Risso G, Sakovsky M, Ermanni P. A highly multi-stable meta-structure via anisotropy for large and reversible shape transformation. Adv Sci 2022;9(26):2202740. http://dx.doi.org/10.1002/advs.202202740.

[11] Shan S, Kang SH, Wang P, Qu C, Shian S, Chen ER, et al. Harnessing multiple folding mechanisms in soft periodic structures for tunable control of elastic waves. Adv Funct Mater 2014;24(31):4935–42. http://dx.doi.org/10.1002/adfm.201400665.

[12] Azulay R, Combescure C, Dirrenberger J. Instability-induced pattern generation in architectured materials — A review of methods. Int J Solids Struct 2023;112240. http://dx.doi.org/10.1016/j.ijsolstr.2023.112240.

[13] Bertoldi K, Vitelli V, Christensen J, Van Hecke M. Flexible mechanical metamaterials. Nat Rev Mater 2017;2(11):1–11.

[14] Siéfert E, Reyssat E, Bico J, Roman B. Bio-inspired pneumatic shape-morphing elastomers. Nat Mater 2019;18(1):24–8.

[15] Gao T, Siéfert E, DeSimone A, Roman B. Shape programming by modulating actuation over hierarchical length scales. Adv Mater 2020;32(47):2004515.

[16] Rafsanjani A, Bertoldi K, Studart AR. Programming soft robots with flexible mechanical metamaterials. Science Robotics 2019;4(29):eaav7874.

[17] Hamouche W, Maurini C, Vincenti A, Vidoli S. Basic criteria to design and produce multistable shells. Meccanica 2016;51(10):2305–20. http://dx.doi.org/10.1007/s11012-016-0375-5.

[18] Haghpanah B, Salari-Sharif L, Pourrajab P, Hopkins J, Valdevit L. Multistable shape-reconfigurable architected materials. Adv Mater 2016;28(36):7915–20. http://dx.doi.org/10.1002/adma.201601650.

[19] Yang H, Ma L. 1D to 3D multi-stable architected materials with zero Poisson's ratio and controllable thermal expansion. Mater Des 2020;188:108430. http://dx.doi.org/10.1016/j.matdes.2019.108430.

[20] Zhang Y, Restrepo D, Velay-Lizancos M, Mankame ND, Zavattieri PD. Energy dissipation in functionally two-dimensional phase transforming cellular materials. Sci Rep 2019;9(1):12581. http://dx.doi.org/10.1038/s41598-019-48581-8.

[21] Qi J, Chen Z, Jiang P, Hu W, Wang Y, Zhao Z, et al. Recent progress in active mechanical metamaterials and construction principles. Adv Sci 2022;9(1):2102662. http://dx.doi.org/10.1002/advs.202102662.

[22] Yang H, D'Ambrosio N, Liu P, Pasini D, Ma L. Shape memory mechanical metamaterials. Mater Today 2023. http://dx.doi.org/10.1016/j.mattod.2023.04.003.

[23] Riley KS, Ang KJ, Martin KA, Chan WK, Faber JA, Arrieta AF. Encoding multiple permanent shapes in 3D printed structures. Mater Des 2020;194:108888.

[24] Riley KS, Le Ferrand H, Arrieta AF. Modeling of snapping composite shells with magnetically aligned bio-inspired reinforcements. Smart Mater Struct 2018;27(11):114003.

[25] Le Ferrand H, Studart AR, Arrieta AF. Filtered mechanosensing using snapping composites with embedded mechano-electrical transduction. ACS Nano 2019;13(4):4752–60.

[26] Emam SA, Inman DJ. A review on bistable composite laminates for morphing and energy harvesting. Appl Mech Rev 2015;67(6):060803.

[27] Vangbo M. An analytical analysis of a compressed bistable buckled beam. Sensors Actuators A 1998;69(3):212–6. http://dx.doi.org/10.1016/S0924-4247(98)00097-1.

[28] Cazottes P, Fernandes A, Pouget J, Hafez M. Bistable buckled beam: modeling of actuating force and experimental validations. 2009.

[29] Camescasse B, Fernandes A, Pouget J. Bistable buckled beam: Elastica modeling and analysis of static actuation. Int J Solids Struct 2013;50(19):2881–93.

[30] Cleary J, Su H-J. Modeling and experimental validation of actuating a bistable buckled beam via moment input. J Appl Mech 2015;82(5):051005.

[31] Faber JA, Udani JP, Riley KS, Studart AR, Arrieta AF. Dome-patterned metamaterial sheets. Adv Sci 2020;7(22):2001955.

[32] Udani JP, Arrieta AF. Programmable mechanical metastructures from locally bistable domes. Extreme Mech Lett 2021;42:101081.

[33] Brinkmeyer A, Santer M, Pirrera A, Weaver P. Pseudo-bistable self-actuated domes for morphing applications. Int J Solids Struct 2012;49(9):1077–87.

[34] Holmes DP, Crosby AJ. Snapping surfaces. Adv Mater 2007;19(21):3589–93.

[35] Toma M, Tawa K. Plasmonic coloration of silver nanodome arrays for a smartphone-based plasmonic biosensor. Nanoscale Adv 2019;1(9):3699–708.

[36] Alturki M, Burgueño R. Response characterization of multistable shallow domes with cosine-curved profile. Thin-Walled Struct 2019;140:74–84. http://dx.doi.org/10.1016/j.tws.2019.03.035.

[37] Udani JP, Arrieta AF. Taming geometric frustration by leveraging structural elasticity. Mater Des 2022;221:110809. http://dx.doi.org/10.1016/j.matdes.2022.110809.

[38] Brodland GW, Cohen H. Deflection and snapping of spherical caps. Int J Solids Struct 1987;23(10):1341–56. http://dx.doi.org/10.1016/0020-7683(87)90001-1.

[39] Kaplan A, Fung Y. A nonlinear theory of bending and buckling of thin elastic shallow spherical shells. Tech. rep., 1954.

[40] Madhukar A, Perlitz D, Grigola M, Gai D, Jimmy Hsia K. Bistable characteristics of thick-walled axisymmetric domes. Int J Solids Struct 2014;51(14):2590–7. http://dx.doi.org/10.1016/j.ijsolstr.2014.03.022.

[41] Taffetani M, Jiang X, Holmes DP, Vella D. Static bistability of spherical caps. Proc R Soc A 2018;474(2213):20170910. http://dx.doi.org/10.1098/rspa.2017.0910, Publisher: Royal Society.

[42] Sobota PM, Seffen KA. Effects of boundary conditions on bistable behaviour in axisymmetrical shallow shells. Proc R Soc A 2017;473(2203):20170230. http://dx.doi.org/10.1098/rspa.2017.0230, Publisher: Royal Society.

[43] Wan G, Cai Y, Liu Y, Jin C, Wang D, Huang S, et al. Bistability in popper-like shells programmed by geometric defects. Extreme Mech Lett 2021;42:101065. http://dx.doi.org/10.1016/j.eml.2020.101065.

[44] Liu T, Chen Y, Liu L, Liu Y, Leng J, Jin L. Effect of imperfections on pseudo-bistability of viscoelastic domes. Extreme Mech Lett 2021;49:101477. http://dx.doi.org/10.1016/j.eml.2021.101477.

[45] Liu M, Domino L, de Dinechin ID, Taffetani M, Vella D. Snap-induced morphing: From a single bistable shell to the origin of shape bifurcation in interacting shells. J Mech Phys Solids 2022;105116. http://dx.doi.org/10.1016/j.jmps.2022.105116.

[46] Rothemund P, Ainla A, Belding L, Preston DJ, Kurihara S, Suo Z, et al. A soft, bistable valve for autonomous control of soft actuators. Science Robotics 2018;3(16):eaar7986. http://dx.doi.org/10.1126/scirobotics.aar7986.

[47] Zhang X, Oseyemi AE, Ma K, Yu S. Entirely soft valve leveraging snap-through instability for passive flow control. Sensors Actuators B 2022;367:132035. http://dx.doi.org/10.1016/j.snb.2022.132035.

[48] Osorio JC, Tinsley C, Tinsley K, Arrieta AF. Manta ray inspired multistable soft robot. In: 2023 IEEE international conference on soft robotics. 2023, p. 1–6. http://dx.doi.org/10.1109/RoboSoft55895.2023.10122038.

[49] Osorio JC, Morgan H, Arrieta AF. Programmable multistable soft grippers. In: 2022 IEEE 5th international conference on soft robotics. 2022, p. 525–30. http://dx.doi.org/10.1109/RoboSoft54090.2022.9762120.

[50] Morgan H, Osorio JC, Arrieta AF. Towards open loop control of soft multistable grippers from energy-based modeling. In: 2023 IEEE international conference on soft robotics. 2023, p. 1–6. http://dx.doi.org/10.1109/RoboSoft55895.2023.10121986.

[51] Preston DJ, Rothemund P, Jiang HJ, Nemitz MP, Rawson J, Suo Z, et al. Digital logic for soft devices. Proc Natl Acad Sci 2019;116(16):7750–9. http://dx.doi.org/10.1073/pnas.1820672116.

[52] Mukherjee A, Risso G, Ermanni P. Quantifying the strength of stability of multi-stable structures: A new design perspective. Thin-Walled Struct 2023;189:110921. http://dx.doi.org/10.1016/j.tws.2023.110921.

[53] Loukaides EG, Smoukov SK, Seffen KA. Magnetic actuation and transition shapes of a bistable spherical cap. Int J Smart Nano Mater 2014;5(4):270–82. http://dx.doi.org/10.1080/19475411.2014.997322, Publisher: Taylor & Francis.

[54] Seffen KA, Vidoli S. Eversion of bistable shells under magnetic actuation: a model of nonlinear shapes. Smart Mater Struct 2016;25(6):065010. http://dx.doi.org/10.1088/0964-1726/25/6/065010, Publisher: IOP Publishing.

[55] Abdullah AM, Braun PV, Hsia KJ. Programmable shape transformation of elastic spherical domes. Soft Matter 2016;12(29):6184–95. http://dx.doi.org/10.1039/C6SM00532B.

[56] Hooshmand-Ahoor Z, Tarantino MG, Danas K. Mechanically-grown morphogenesis of Voronoi-type materials: Computer design, 3D-printing and experiments. Mech Mater 2022;173:104432. http://dx.doi.org/10.1016/j.mechmat.2022.104432.

[57] Rivlin RS, Rideal EK. Large elastic deformations of isotropic materials IV. further developments of the general theory. Philos Trans R Soc Lond Ser A Math Phys Sci 1948;241(835):379–97. http://dx.doi.org/10.1098/rsta.1948.0024, Publisher: Royal Society.

[58] Abaqus. 2022, URL http://130.149.89.49:2080/v6.10/books/usb/default.htm?startat=pt05ch19s05abm07.html.

[59] Riks E. An incremental approach to the solution of snapping and buckling problems. Int J Solids Struct 1979;15(7):529–51. http://dx.doi.org/10.1016/0020-7683(79)90081-7.

[60] Becque J, Rasmussen KJR. Numerical investigation of the interaction of local and overall buckling of stainless steel I-columns. J Struct Eng 2009;135(11):1349–56. http://dx.doi.org/10.1061/(ASCE)ST.1943-541X.0000052.

[61] Stratasys. 2021, URL https://support.stratasys.com/en/printers/polyjet-legacy/eden260v-vs.

[62] Zerhouni O, Tarantino MG, Danas K. Numerically-aided 3D printed random isotropic porous materials approaching the Hashin–Shtrikman bounds. Composites B 2019;156:344–54.

[63] Tarantino MG, Zerhouni O, Danas K. Random 3D-printed isotropic composites with high volume fraction of pore-like polydisperse inclusions and near-optimal elastic stiffness. Acta Mater 2019;175:331–40.

[64] Zaccaria D, Bigoni D, Noselli G, Misseroni D. Structures buckling under tensile dead load. Proc R Soc A 2011;467(2130):1686–700.

[65] Combescure C, Elliott RS. Hierarchical honeycomb material design and optimization: Beyond linearized behavior. Int J Solids Struct 2017;115:161–9.

[66] Poincloux S, Vallat C, Chen T, Sano TG, Reis PM. Indentation and stability of woven domes. Extreme Mech Lett 2023;59:101968.

[67] Lee A, López Jiménez F, Marthelot J, Hutchinson JW, Reis PM. The geometric role of precisely engineered imperfections on the critical buckling load of spherical elastic shells. J Appl Mech 2016;83(11):111005.

[68] Jeong HY, An S-C, Seo IC, Lee E, Ha S, et al. 3D printing of twisting and rotational bistable structures with tuning elements. Sci Rep 2019;9(1):324. http://dx.doi.org/10.1038/s41598-018-36936-6, Number: 1 Publisher: Nature Publishing Group.

[69] Danish B, Anilkumar PM, Rao BN. Suppression of cross-well vibrations of a bistable square cross-ply laminate using an additional composite strip. Int J Dyn Control 2023. http://dx.doi.org/10.1007/s40435-023-01153-1.

[70] Wang W, Cao J, Bowen CR, Litak G. Multiple solutions of asymmetric potential bistable energy harvesters: numerical simulation and experimental validation. Eur Phys J B 2018;91(10):254. http://dx.doi.org/10.1140/epjb/e2018-90180-y.